Electrospun carbon fibers as air cathodes for aprotic Li–O2 battery: Towards cathode design for enhanced capacity

Manel Ben Osman, Wei Yin, Thomas Petenzi, Bruno Jousselme, Renaud Cornut, Encarnación Raymundo-Pinero, Christel Laberty Robert, Manel Ben Osman, Alexis Grimaud, Christel Laberty Robert

Electrospun carbon fibers as air cathodes for aprotic Li-O_2 battery: towards cathode design for enhanced capacity

Manel Ben Osman[a], Wei Yin[b], Thomas Petenzi[c], Bruno Jousselme[c], Renaud Cornut[c], Encarnación Raymundo-Pinero[d], Alexis Grimaud[b] and Christel Laberty Robert[a,*].

[a] Sorbonne Université, UPMC Univ Paris 06, CNRS, Collège de France, Chimie de la Matière Condensée de Paris, 75005 Paris, France.
[b] Chimie du Solide et de l'Energie, UMR 8260, Collège de France, 75231, Paris Cedex 05, France.
[c] LICSEN, NIMBE, CEA, CNRS, Université Paris-Saclay, CEA Saclay 91191 Gif-sur-Yvette Cedex, France.
[d] CEMHTI–CNRS Orléans, site haute température, 1D Avenue de la Recherche Scientifique, 45071 Orléans Cedex 02, France.

Key words: Electrospun carbon fibers, Li-O_2 battery, aprotic, cathode

ABSTRACT

This report investigates how the microstructures and chemical properties of carbon cathodes influence ~~on~~ the discharge capacity of aprotic Li-O_2 batteries. For that, electrospun carbon fibers (CFs), Multi-wall carbon nanotubes (MWCNTs), carbon Super P and gas diffusion layer (GDL) were fully discharged at various applied current densities (0.05 - 0.5 mA.cm$^{-2}_{(geom)}$) and characterized by means of ex-situ techniques such as XRD and FEG–SEM. The major discharge product for every carbon electrode was identified as Li_2O_2 by both XRD and gas pressure analysis. The corresponding electrochemical results showed two different behaviors depending on the current density. At high current densities, all the carbon electrodes presented quite similar discharge capacities due to the most favored formation of Li_2O_2 conformal film on the carbon surface. In contrast, at lower current densities, the morphology of the discharge product changed and Li_2O_2 was preferably deposited as micrometer–sized toroïds particles on all the carbon cathodes (except for GDL). In this particular regime, the specific capacity normalized by the active carbon surface area of the electrospun CFs cathode was surprisingly promoted compared to the other carbon materials. Interestingly, it was found that unlike for the other cathode materials, Li_2O_2 homogenously occupies the void volume of the electrospun carbon structure without any pores clogging, which was attributed to its particular macroporous architecture presumably facilitating a continuous O_2 diffusion through the electrode. The enhancement in discharge capacity might also be related to the presence of nitrogen active sites, as revealed by XPS analysis of the pristine carbon surface. All these features highlight that the carbon porosity and surface chemistry are key parameters to design efficient air cathodes for Li-O_2 batteries performing at low current density.

∗ Corresponding author.
Email address : christel.laberty@sorbonne-universite.fr (Christel Laberty-Robert)
LCMCP, Sorbonne Université, 4 place Jussieu, 75005 Paris.

1. Introduction

Non-aqueous Li-O_2 batteries have attracted significant attention over the past decade thanks to their high theoretical specific energy density around 2000 $Wh.kg^{-1}_{(Li + carbon)}$. In comparison to other energy storage devices, including the conventional Li-ion batteries, they could be potentially suitable for electrical vehicles applications [1-3]. This enhancement in specific energy is related to the use of a gas to solid reaction in the pores of a conductive electrode, which is composed by cost effective carbon materials with low densities, and therefore facilitates high gravimetric capacities. During the discharge, O_2 gas is dissolved in the electrolyte and then electrochemically reduced to react with Li^+ ions to form Li_2O_2 as the main product while the reverse reaction occurs during charge, decomposing Li_2O_2 into Li^+ and O_2 (equation A.1).

$$O_2 + 2\,Li^+ + 2\,e^- = Li_2O_2 \quad \text{(Equ. A.1)}$$

Generally, the Li-O_2 reactions involved upon cycling were found to be dependent on the operating parameters of the cells (current density, oxygen pressure…), the nature and the concentration of electrolyte and the presence of electrocatalysts or redox mediators [4-17]. Previous studies have also demonstrated that the solubility of LiO_2 intermediate governs the discharge product morphology [18], varying from films to discs [19] and to toroïds [20], which eventually impacts the battery performance. Besides the peculiar attention recently devoted to the understanding of the fundamental mechanisms controlling the Li-O_2 electrochemistry [21], there is an important consideration in the design and selection of effective porous air cathodes [22]. In fact, the real performance of Li–O_2 batteries including capacity fading, poor cycling and large discharge-charge voltage gap [23] is strongly attributed to the poor performance of the air electrodes because of the sluggish kinetics for oxygen reduction/evolution reactions and the inefficient air electrode design. Thus, one of the major challenge for Li-O_2 batteries is to design porous electrodes that must contain active carbon material providing abundant redox reaction sites and a large connected porous framework. It can be filled up by the Li_2O_2 solid deposit during operation without clogging the pores [24] or passivating electrode surface [21,25], which are phenomena often suggested as the main factors limiting the cell capacity. Numerous carbon materials (e.g. activated carbon [26], Super P [27,28], GDL [29], carbon nanotubes (CNTs) [20], graphene [30], Vulcan XC72, Ketjen black [31,32], carbon paper [33], fibers [34]) were used as performant air cathodes for Li–O_2 applications, due to their low cost, high electrical conductivity, wide chemical and electrochemical stability and to their large specific surface area and high porosity. In addition to carbon materials, several cathode formulations required the use of binders, like PVDF and PTFE [35], which might also react during the discharge processes to form side products, leading to a decrease of the cell performance. One can imagine that playing on the carbon specifications including electronic conductivity, porosity, tortuosity and surface properties is the key strategy to improve the discharge capacity in Li-O_2 cells. However, no systematic investigation has clearly identified the critical carbon properties that impact effectively the Li-O_2 battery performance.

Hence, in this report our approach consists on comparing different carbon cathodes discharged at different rates to identify the key properties required to enhance the Li-O_2 battery electrochemical performance. Using carbon materials with different microstructures (size and porosity) and chemical properties (electrospun fibers (CFs), Multiwall carbon nanotubes (MWCNTs), carbon Super P and gas diffusion layer (GDL)), we systematically investigate the impact of carbon microstructure on the morphology/size and distribution of Li_2O_2 discharge products and thus on the full discharge capacity

values reached at different rates. We employed ex-situ techniques including X-ray diffraction, Raman spectroscopy and FEG-SEM analysis for the structural and morphological characterizations of Li_2O_2 products. The deposition process of Li_2O_2 was found to be correlated with the current density as well as to the carbon nature. Then, we highlighted that at low discharge current densities, when compared with the other carbon materials, the self-standing and binder-free electrospun carbon electrodes composed of more than 90 percent void space and presenting a small surface area exposing active sites for the oxygen reduction reaction (ORR) is a very promising air cathodes as they can store homogeneously the solid Li_2O_2 particles in the entire volume of the carbon. These findings contribute to a new understanding on how the carbon cathode design controls $Li–O_2$ electrochemistry.

2. Experimental Section

2.1. Carbon electrodes

In this work, all the materials (except carbon Super P) are prepared in self-standing form with suitable mechanical strength. The four porous materials that were employed as cathodes to assemble the cells are:

The **Gas Diffusion Layer** (GDL, Freudenberg H2315), here used as cathode (200 µm in thickness, 0.64 cm^2 disc) was obtained from Quintech. It consists of a macroporous and electrically conductive binder free carbon paper that is known to supply fuel cells with the reaction gas.

Electrospun carbon fibers (CFs). Self–standing fibrous carbon papers were prepared via electrospinning followed by heat treatment at high temperatures (Fig. S1). A solution of Polyacrylonitrile (PAN, Sigma Aldrich) with molecular weight of 150,000 g mol^{-1}, one of the most commonly used precursors due to its high carbon content [36,37], is dissolved in dimethylformamide (DMF) solvent at 10 wt. % and extruded with a fixed 0.03 $ml.min^{-1}$ flow rate at 15–18 kV voltage in a sealed box under air flow to control the relative humidity in the atmosphere (RH ≤ 20 %). The distance between the needle tip and the grounded collector is fixed at 13 cm for all the preparation. The volume of the PAN / DMF solution was modulated leading to different membranes thicknesses (400–600 µm). Then, thermal steps are used to obtain carbon fibers from electrospun polymer fibers, following the procedure previously described [38]. Briefly, the polymer-based membranes are first dried at 70 °C under air to evaporate the residual DMF before to be stabilized at 280 °C under oxidizing atmosphere (i.e., air) to prevent further mass loss resulting from the fiber fusion / degradation at high temperatures in inert atmosphere. This step is critical to have fibers with good tensile strength. Finally, membranes are carbonized at 950 °C under argon to attain the graphitic structure and to produce conductive carbon, as confirmed by XRD and Raman studies (Fig. S2). After the carbonization process, the fibers diameter is reduced by 30 % due to the removal of non–carbon elements. The final electropsun carbon membrane is self–standing with very suitable mechanical resistance for use. The 600 µm final electrospun carbon cathode denoted CF wt.% PAN was cut into a 0.64 cm^2 disc with the mass loading of 2 $mg.cm^{-2}$ approximately.

Multi-Wall Carbon Nanotubes electrode. First, 80 mg of MWCNTs (Nanocyl SA-NC7000, 10 ± 2 nm in diameter) was dispersed in absolute ethanol and the resulting suspension was sonicated several times during 3 hours, increasing successively the volume of solvent. This latter was filtrated under vacuum on a PTFE membrane (Sartorius, pores diameter = 0.45 µm) and dried at room temperature (RT) overnight. MWCNT membrane is taken off from the PTFE surface to be self-standing and the carbon nanotube loading is 2.0 $mg.cm^{-2}$. The as–prepared membrane with a thickness of 80 µm was punched into a 0.64 cm^2 disc.

Super P carbon. Super P carbon electrode was prepared by the drop-casting method, as previously reported [39]. Briefly, 90 wt. % Carbon Super P (Csp, Timcal Ltd) and 10 wt. % polytetrafluorethylene (PTFE, 60 wt. % dispersion in water, Sigma-Aldrich) were mixed in a certain amount of isopropanol (≥ 99.9 %, Sigma-Aldrich) to prepare a slurry. This one was then deposited onto 11 mm diameter stainless steel meshes (AISI 316, 325 mesh, 0.036 mm diam wire, Alfa Aesar). After being dried in ambient air and washed with a water/ethanol (v/v = 1:2) solution to remove the surfactants in the PTFE dispersion, these electrodes were further dried overnight at 80 °C under vacuum in BÜCHI oven and stored in glove box. Carbon Super P loading of the resulting electrodes is 0.3 (± 0.02) mg with a surface area of 0.4 (± 0.04) cm^2.

2.2. Carbon electrode characterizations

X-ray diffraction (XRD) was used to investigate the crystallinity of the carbon cathodes and to identify the crystalline nature of the discharge products. A Bruker D8 Advance diffractometer with a Cu Kα radiation source (λ1 = 1.5405 Å, λ2 = 1.5443 Å) and a Lynxeye XE detector was used to collect the XRD patterns. The XRD patterns corresponding to the discharged electrodes were recorded for 40 min in the 2θ range of 30 – 70 °C at a continuous scan rate of 1° min^{-1}, using an airtight sample holder with beryllium windows. Concerning the pristine electrodes, the XRD patterns were collected for 15 min with a scan rate of 4° min^{-1}.

Raman spectra were recorded using a custom–built confocal Raman microscope with a 50 × 0.45 NA objective (Nikon). The Raman system was equipped with a 473 nm diode laser (Sacher Lasertechnik) and a spectrometer (Shamrock SR-303i, Andor Technology) which employed a 400 lines/mm grating, blazed at 850 nm and was equipped with a deep depletion, back-illuminated, and thermoelectrically cooled CCD camera (Newton, Andor Technology) for the detection of the Raman signal. A silicon wafer was used for calibration.

The porous texture of the materials was analyzed by N_2 adsorption at 77 K (Quadrasorb, Quantachrome, USA) and mercury intrusion porosimetry (Autopore IV, Micromeritics, USA). It is worthy to precise that the fibers are dense and the major porosity discussed in these materials is defined by the presence of inter–fiber spaces/voids. Prior to the N_2 adsorption measurements, the samples were outgassed at 120 °C for 12 h under vacuum. The micropore and mesopore volumes and the pore size distribution were determined by a Non–Local Density Functional Theory method (NLDFT) with a slit shape pore model applied on N_2 adsorption data. The meso– and macro–pore size distributions from mercury intrusion porosimetry were obtained from the pressure versus intrusion data using the Washburn equation.

Microscopic observations were performed by field emission gun–scanning electron microscopy (FEG–SEM) on a Hitachi SU–70 instrument which is provided with a Schottky Field Effect gun. Because of the extreme sensitivity of samples to electron beam, low accelerating voltage (1 kV) and low beam current conditions were selected to avoid any possible destruction of the discharge product. Conditions for secondary electron (SE) imaging were high resolution mode with the upper detector resulting in a narrow energy band filtering for out coming SE, as a consequence dielectrical properties of the different materials constituting the sample resulted in highlighted contrast. The SEM images of the pristine carbon electrodes are presented in Fig. S3 and the size distribution of the fibers was determined from these pictures using the ImageJ software. The discharged samples were transferred into the SEM under anaerobic conditions.

X–ray Photoelectron Spectroscopy (XPS) measurements were carried out to assess the surface chemical composition of the pristine carbon electrodes. The XPS spectra were collected on an

Omicron Argus X–ray photoelectron spectrometer, using a monochromated Al Kα (hα = 1486.6 eV) radiation. The emission of photoelectrons from the sample was analyzed at a take–off angle of 45° under ultrahigh vacuum conditions (1.10^{-9} Pa). XPS spectra were collected at pass energy of 20 eV for C1s, O1s, N1s, core XPS levels. The area of the sample analysis is approximately 1 mm^2. All binding energy (BE) values were charge-corrected to the carbon C1s excitation set at 285.0 eV. The peak areas were determined after subtraction of a Shirley background. The atomic ratios calculations were performed after normalization using Scofield factors. Spectrum processing was carried out using the Casa XPS software package.

The contact angle experiments were carried out by dropping an electrolyte droplet on the carbon surfaces. Measurements were repeated three times. The electrolyte uptake which is one of the important characteristic properties for the carbon wettability behavior was estimated by soaking a precise volume of the electrolyte solution into the electrodes. The electrolyte excess was wiped off gently with a porous paper on both sides and the carbon materials were then weighted immediately. The electrolyte uptake (%) was calculated using the following equation [40].

$$\text{Electrolyte uptake} = [(W_{wet} - W_{dry})/ W_{dry}]*100\%$$

where W_{wet} and W_{dry} are the weights of the electrolyte-swollen and dry carbon sample, respectively.

The electronic resistivity of the O_2 cathodes was measured by the four-probe technique (Jandel, Model RM3000). Additionally, they were also examined by electrochemical impedance spectroscopy (Solartron SI 1260, impedance/ Gain-phase analyzer) in Swagelock cells with an AC amplitude of 100 mV and a frequency ranging from 100 to 0.01 kHz.

2.3. Electrochemical characterization

Li-O_2 cells assembling and testing. Prior to use, Dimethoxyethane (DME) solvent was dried with freshly activated molecular sieves (4 Å) for two days. Lithium salt was dried under vacuum at 80 °C for 12 – 24 h. The 0.1 M electrolyte solution was prepared in an argon-filled glovebox (0.1 ppm of O_2/0.1 ppm of H_2O). The water content in the electrolyte solutions was analyzed by Karl Fischer titration and found to be below 10 ppm. Before electrochemical experiments, the carbon electrodes were dried under vacuum at 80 °C for 24 h. The pressure cells used in this work were previously described [39]. The cells were assembled in an Ar–filled glovebox (0.1 ppm of O_2/0.1 ppm of H_2O) using a Li metal foil anode (cut into a 0.64 cm^2 disc, 9 mm diameter), two Whatman porous glass fibers separators (dried under vacuum at 260 °C for 8 h), wetted with 300 µL of the electrolyte (0.1 M $LiPF_6$ dissolved in DME) and a binder free air cathode consisting of self–standing carbon (electrospun fibers mat, MWCNT carpet, GDL, cut into a 0.64 cm^2 disc) or carbon Super P deposited on stainless steel mesh by drop casting. Stainless steel mesh was used as current collectors. The assembled cells were transferred from the glovebox, first evacuated before to be filled with dry and ultrapure gaseous O_2 (a pressure of ca. 1.6 bar has been set for all the tests). Cells are left at the open circuit voltage (OCV = 3.3 V) for 10 hours under temperature-controlled conditions (25 °C ± 0.1 °C fixed by an incubator) in order to ensure the homogeneity of the gas atmosphere and the full wetting of the electrode. The discharge measurements were carried out in galvanostatic conditions with cut off voltage of 2 V vs. $E°_{Li/Li+}$ using a Bio–Logic VMP3 potentiostat at different current densities in the range of 0.05–0.5 $mA.cm^{-2}_{(geom)}$. The current density is estimated on the basis of the geometric surface of the electrode (0.64 cm^2) fixed for every measurement. The total weight of the carbon electrodes (g_c) before discharge was used for capacity normalization. Besides the electrochemical data, the pressure analysis and e^-/O_2 ratios were calculated as described elsewhere [39]. The electrospun carbon fibers prepared from 10 wt.% PAN/DMF content were used in cells that are fully

discharged with a current density of 0.05 $mA.cm^{-2}_{(geom)}$. Each cell test was repeated three times to ensure the data reproducibility (example of CF–10 wt.% PAN discharged at 0.05 $mA.cm^{-2}_{(geom)}$ are displayed in Figure S4). Generally, the standard deviation calculated from the capacities values obtained for three cells is approximately 200 $mA.h.g_c^{-1}$.

For post–mortem analysis (XRD, FEG–SEM) of carbon electrodes, the discharged Li-O_2 cells were first transferred without any exposure to ambient air to an Ar-filled glovebox and disassembled. Prior to the characterizations, the discharged cathodes were washed three times with dimethoxyethane (DME) to remove the electrolyte residues and dried in a vacuum chamber at RT for 15 min before analysis.

3. Results and discussion

To compare the electrochemical performances of the different carbon electrodes, discharges at different rates were made using a normalized current density by the geometrical surface area which is similar for every carbon (varying from 0.05 to 0.5 $mA.cm^{-2}_{(geom)}$). Fig. 1a presents typical discharge voltage curves for Li–O_2 cells employing electrospun carbon cathodes at different rates. The electrochemical profiles of the other carbon cathodes were reported in Fig. S5. Whatever the nature of the carbon electrode, the discharge capacity and the discharge voltage decrease, when increasing the current density. At low current density, the discharge voltage is constant and closer to the thermodynamical potential for Li_2O_2 (2.96 V vs. Li^+/Li) [41]. The formation of Li_2O_2 as a discharge product [42,43] was confirmed by post–mortem XRD patterns in which characteristic peaks for crystalline Li_2O_2 could be observed for CFs, MWCNT and carbon Super P electrodes discharging at different rates (Fig. 2a). For GDL electrodes, no crystalline Li_2O_2 could be identified as a discharge product, in agreement with the limited discharge capacity achieved with this type of carbon electrode.

Fig. 1. (a) Full discharge voltage profiles of the electrospun carbon electrode at different discharge rates. Variation of the full discharge capacities reached for the different carbon materials as a function of current density applied in Li–O_2 cells using 0.1 M $LiPF_6$ in DME. The capacities values were normalized by (b) the total carbon cathode weight (g_c) or (c) the geometric cathode surface (0.64 cm^2) or (d) the active surface area (m_c^2) calculated on the basis of the estimated surface area ($m^2.g^{-1}$) in table 1 and the carbon weight (g_c).

Concomitantly, the cell pressure changes related to the O_2 consumption during the discharge process (Fig. S6) show for CFs, MWCNT and carbon Super P based cells a nearly 2e- /O_2 ratio, consistent with the formation of Li_2O_2 following equation (1) (Fig. 2b). In contrast, for the GDL cathode, a very low consumption of O_2 was detected, as expected from the poor performance observed for this electrode (≤ 10 $mA.h.g_c^{-1}$) at different discharge rates.

As can be seen in Fig. 1a and S5, the electrochemical behaviors of the cells at the different discharge rates are strongly dependent on the carbon electrodes, which require a deeper fundamental understanding of the intrinsic properties of each carbon. For that, the discharge capacities normalized by the geometric electrode surface, the mass of carbon and the active surface area of carbon (taking into account the specific surface area and the carbon mass) were compared (Fig. 1b, 1c, 1d). At low current densities corresponding to 0.05 $mA/cm^2_{(geom)}$, carbon Super P electrodes exhibit the highest capacity value normalized by the geometric electrode surface or the mass of carbon. However, especially at high current densities the MWCNTs cathodes can be considered as the best performant carbon cathode as they deliver higher capacity normalized by the geometric electrode surface or the mass of carbon. Looking at the capacities normalized by the active carbon

surface area (Fig. 1d), two regimes are observed at low and large current densities. At low current densities, the electrospun carbon cathode delivered a capacity greater by a factor of 6 when compared to the other materials, which is not the case if we normalize by the geometric electrode surface or the mass of carbon. However, at large current densities ≥ 0.2 $mA.cm^{-2}_{(geom)}$, quite similar discharge capacities were obtained for all the carbon electrodes, which raised the question to know if in this regime only the surface of the electrode is used or the whole porosity available for electrochemical reactions. To explain this behavior, microscopic studies were performed on the discharged cathodes at the different rates across the whole carbon thickness to investigate the impact of the carbon microstructure on the Li_2O_2 deposits in terms of their morphology, size and homogeneity of dispersion.

Fig. 2. (a) XRD patterns of the cathodes after full discharge at 0.05 $mA.cm^{-2}_{(geom)}$. (b) Gas evolution profiles of Li–O_2 cells at low current density of 0.05 $mA.cm^{-2}_{(geom)}$ using 0.1 M $LiPF_6$ in DME, the ratio of number of electrons to oxygen is very close to 2.

~~In~~ Fig. 3 reported the FEG–SEM images of all the carbon materials at the O_2 / cathode interface after full discharge at different current densities, whose corresponding discharge curves were presented in Fig.1. Two morphologies (toroïds vs. film) for Li_2O_2 particles were observed as a function of the current density. At high current densities, despite the formation of few small toroïds shaped particles, one could observe a conformal film covering the entire surface of every carbon electrode (Fig. 3a). This morphology is in line with the quite similar discharge capacities obtained in this regime for these different electrodes. However, at low current densities, well-defined Li_2O_2 toroïds are formed on the carbon surfaces by stacking thin layers / platelets of Li_2O_2 products during the course of the discharge process. These observations are in agreement with the reported morphology of Li_2O_2 formed in ether-based electrolytes during discharge [20,44]. The formation of toroïds with hundreds of nanometers is known to result from a solution mechanism and these particles could be more favorable for achieving high capacity cathodes as it was reported earlier [45,47]. For GDL electrode, regardless of the current density, a continuous amorphous thin film (≈ 10 nm) is homogeneously formed with some small agglomerates (Fig. 3b). Such a film formation, resulting from a surface mediated mechanism [42], indicates the electrical passivation of the GDL which is coherent with the rapid death of the cells exhibiting very low capacities and poor rate capability (Fig. 1).

Fig. 3. (a) Morphology of Li_2O_2 products formed at the O_2/cathode interfaces during full discharge step of carbon materials in Li-O_2 cells at different current densities using 0.1 M $LiPF_6$ in DME. (b) Representative microscopic images of fully discharged GDL cathode regardless of the current density applied in the cell.

Based on these features, we can emphasize the effect of current density on the nucleation and growth kinetics of solid Li_2O_2 onto the carbon electrodes. Indeed, when the current density is increased, the size of the toroïds decreases which results in lower discharge capacities. For high current densities, independently of the carbon surface, the discharge takes place quickly and the nucleation from solvated precursors becomes faster than the growth, leading to the formation of conformal Li_2O_2 films. Certainly, in this regime, we can suggest that the Li_2O_2 morphology is the main parameter governing the capacity performance for all the carbon electrodes. At lower current densities, although the diffusion of the species should enhance the uniform growth of bigger particles, any subtle differences in the Li_2O_2 morphology cannot justify the very important capacity

normalized by the active carbon surface area delivered by the electrospun carbon cathode when compared to the other carbon materials (≤ 0.1 $mA.cm^{-2}_{(geom)}$).

For further information, complementary FEG–SEM observations were carried out at the separator / cathode interfaces and through the carbon cathodes (cross section) discharged at 0.05 $mA.cm^{-2}_{(geom)}$ (Fig. 4 and Fig. S7).

Fig. 4. Distribution of Li_2O_2 products formed through the carbon cathode volume during full discharge step in Li-O_2 cells at low current density of 0.05 $mA.cm^{-2}_{(geom)}$.

The images confirm that any morphological differences between the different carbons are retained along the electrodes thickness and the formation of Li_2O_2, as conformal coatings or toroïds occurs throughout the electrodes. This result implies that the Li–O_2 reactions are not limited to the carbon surface but all the carbon volume is participating as Li_2O_2 deposits are present in the entire volume of the electrodes. Note that the utilization of the carbon volume was confirmed for all the current densities (Fig. S7). More interestingly, the Li_2O_2 discharge product is uniformly distributed as toroïds in the volume of the electrospun cathode with a constant particle size. However, for MWCNT at 0.05 $mA.cm^{-2}_{(geom)}$, the morphology of Li_2O_2 deposit is not uniform: Li_2O_2 toroïds with 1.2 µm in diameter are deposited on the top surface of MWCNT cathode, while smaller toroïds with 800 nm in diameter were observed at the electrolyte/electrode interface. In the center of the electrode, the discharge product is a conformal film along the MWCNT sidewalls (Fig. 4). When considering carbon Super P cathode, similar tendencies as for MWCNT cathode are obtained. Hence, globally we notice that in MWCNT and carbon Super P cathodes the larger Li_2O_2 particles are preferentially formed at the O_2 interface rather than the electrolyte interface. All these observations suggest a diffusion limitation in the porosity of the MWCNT and carbon Super P cathodes, leading to heterogeneous distribution of Li_2O_2 compared to electrospun carbon, which could be related to the inhomogeneous distribution of gaseous oxygen or Li+ in the electrode owing to the tortuosity of the conductive network. These features reveal that the size and distribution of Li_2O_2 toroïds formed in MWCNT and carbon Super P cathodes are highly dependent on the local concentration of reactant, either O_2 or Li^+, suggesting that the whole carbon volume in these cathodes was not efficiently used to accommodate the discharge product in its porosity, in contrast to electrospun carbon cathode.

In order to reveal the effect of pores size and/or porosity volume on this limitation, mercury porosity experiments have been performed on the pristine carbon electrodes and the results are reported in Table 1.

Table 1
Surface and porosity characteristics of pristine carbon electrodes.

These experiments highlight that the electrospun carbon (CFs) electrode exhibits an open porous structure with large macropores volume (34.8 $cm^3.g^{-1}$) and pore size (mean pore diameter of 1 –1.5 µm). This result might explain the homogenous distribution of Li_2O_2 resulting from a faster O_2 diffusion from the oxygen side to the separator side in the entire electrode. Nevertheless, the narrower pore diameter for the other materials could impede the oxygen diffusion and lithium ion movement leading to pores clogging rather than a complete filling, alike previously reported for mesoporous gas diffusion electrodes (GDE) [48]. As a result, the discharge products are formed preferentially at the top and on the bottom of the electrode while the pore volume in the bulk was not used. The particular CF microstructure makes such a carbon paper a very interesting support for Li_2O_2 discharge product. Furthermore, it is worthy to note that although the electrospun carbon

collected at the end of the full discharge presents a quite filled porosity with Li_2O_2 particles, we can observe some empty voids which could mean that in contrast to what is assumed by the majority of studies, the pores clogging is not the main reason of the cell death. The limiting factor of this carbon material is probably due to other parameters such as the poor electronic conductivity of Li_2O_2 [1,49,50] and not to the oxygen diffusion limitations since free space is still available and the diameter of Li_2O_2 toroïds is inferior to the pore size.

Since the oxygen seems to diffuse freely throughout the electrospun cathode volume, the impact of the CFs electrode thickness has then been tested, aiming to improve the discharge capacity. To do so, we adjusted the electrospinning parameters to fabricate thicker electrodes ranging from 400 to 600 µm. Thicker electrospun carbon electrodes (> 600 µm) were not investigated since they might present wettability issues with the electrolyte in the whole carbon volume. Fig. 5 shows that thicker cathode exhibits higher capacity and larger amounts of Li_2O_2 toroïds deposited in the entire carbon volume.

Fig. 5. (a) Full discharge voltage profiles of electrospun carbon fibers (CF_10% PAN) with different thicknesses in Li-O_2 cells operating at 0.05 mA.cm$^{-2}_{(geom)}$) using 0.1 M $LiPF_6$ in DME. (b) FEG–SEM analyses of the fully discharged 600 µm–CF cathode.

As the weight of the thicker cathode is not proportional to the thickness, the density is decreasing with the thickness and therefore the thicker electrode presents the most open porosity. Having more carbon active surface area associated with more available pores volume in thicker cathodes leads to the enhancement of the capacity (in mA.h.g$^{-1}_{carbon}$). The same trend was observed if we consider the capacity value normalized by the active carbon surface area (in mA.h.m_c^{-2}) (Fig. S8).

Moreover, microscopic analysis confirmed this result as the Li_2O_2 toroïds were covering the entire thickness of the cathode (Fig. 5b). These experiments highlight that the electrospun carbon fibers acting as O_2 cathode without any binder or catalyst are good alternatives to improve the energy and power density of Li–O_2 batteries.

Aside from the carbon microstructure factor, other physico–chemical factors (wettability, the conductivity of the electrodes and the chemical composition of the carbon electrodes) might also influence the electrochemical behaviours. In one hand, the contact angle measurements (not shown here) revealed no notable differences between CF and the other cathodes, therefore, the contribution of the wettability factor can be excluded to explain the differences in the capacity performance.

On the other hand, the study of intensity ratio I_D/I_G, characteristic of the carbon structure and conventionally used to estimate the degree of the carbon materials graphitization, showed that GDL has the lowest I_D/I_G ratio indicating then a higher graphitic structure (Fig. S9) which is in line with its higher electronic conductivity value. According to the total electronic conductivity of the investigated carbon materials measured by four probe technique (surface) and impedance spectroscopy (bulk) (Table 2), it can be stated that GDL with good electronic conductivity properties presents the lowest discharge capacity. This finding reveals that the differences in performance cannot be directly related to the materials' conductivity properties.

Table 2
Electronic conductivities values of carbon electrodes.

The chemical composition of the pristine carbon surfaces was finally evaluated by XPS (Fig. 6a). The data show mainly carbon (90–99%) and very small amounts of oxygen and nitrogen. Although the

amount of surface oxygen groups is quite similar for GDL, CF electrode and carbon Super P, MWCNT cathode exhibits a very limited concentration of this type of sites. Furthermore, the CF electrode exhibits the highest nitrogen content (7 %), suggesting that nitrogen functional groups remain at the surface (from polyacrylonitrile, PAN) due to the relatively low carbonization temperature (below 1300°C). Note that no traces of nitrogen groups were detected for MWCNT and carbon Super P samples.

Fig. 6. (a) XPS spectra of the different carbon electrodes with the related surface chemical composition. The binding energies for carbon, nitrogen and oxygen are 284.8, 389.32 and 533 eV, respectively. (b) XPS deconvolution of N1s peaks of carbon cathodes before discharge. N-1, N-2 and N-3 correspond to Pyridinic-N (BE = 398.3 eV), Pyrrolic-N (BE = 400.9 eV) and Graphitic–N (BE = 403.5 eV), respectively. (c) XPS analysis of the C1s region in carbon materials before discharge showing different chemical bonds sp^3, sp^2 and oxygen species present in different relative proportions. Carbon sp^2 (BE= 284.8 eV), carbon sp^3 (BE= 285.7 eV), C-O (BE=287.7 eV), C=O and/or C=N (BE= 289 eV) and shake up π-π* (BE=290.7 eV). The peak lineshapes used were Voigt functions, i.e. Gaussian–Lorentzian convolutions, with an integral background subtracted prior to fitting. The peaks assignments were based on models discussed in [51].

Therefore, we can suggest that the increasing of nitrogen functional groups, known as active sites for ORR [52], could be also related to the performance enhancement. Nitrogen doped carbon materials for high performing lithium air batteries are already well outlined in the literature [53]. One can note that in the N1s spectra region (Fig. 6b), the relative amounts of pyridinic–N, and pyrrolic–N are different in CF–10%PAN and GDL electrodes. The electrospun CF has a higher amount of pyridinic–N than pyrrolic–N compared to GDL and presents also a supplementary contribution attributed to graphitic–N. Furthermore, the C speciation for the electrospun CF and GDL electrodes were determined (figure 6c). The C1s spectra reveal the presence of five peaks corresponding to carbon sp^2, carbon sp^3, C-O, C=O and/or C=N and shake up π-π*. After deconvolution of the C1s spectra, we can notice that the relative amounts of carbon sp^2 and carbon sp^3 are different from one sample to another. The amount of the unsaturated carbon atoms is relatively higher in the electrospun carbon cathode which might be related to the presence of structural defects as introduced by the nitrogen atoms. One can hypothesize that the difference in the nature of the N sites and the related structural defects can explain the higher discharge capacity normalized by the active carbon surface area of the electrospun CFs compared to GDL electrode. Such hypothesis is supported by the recent strategy consisting in the N-doping of carbon materials to covalently anchor some electrocatalytically active sites serving to enhance the discharge capacity [12]. In our work, the presence of more nitrogen groups, associated with the suitable microstructure and porosity are revealed as the key parameters to explain why the CF electrode was more efficient when discharging at lower current density, leaving aside the addition of electrocatalysts. Hence, we can conclude that the electrospinning is a simple and an efficient way to obtain a carbon electrode with an optimized pores volume and size required to balance the surface area and the diffusion of the reactants (Li^+, O_2), thus preventing the pores clogging by the discharge products. Besides, a further functionalization of the carbon surface via heat or acid treatments could be very useful to increase defects or reactive sites for the nucleation and growth of discharge products.

4. Conclusions

In this work, the full discharge profiles and capacities of aprotic Li-O_2 batteries were discussed in relation with the intrinsic physico–chemical properties of various carbon materials (electrospun fibers, GDL, MWCNTs and carbon Super P) used as O_2 cathodes at different current densities. These

investigations aim at identifying the critical parameters controlling the electrochemical behaviors of the carbon cathodes discharged at different rates. The ex–situ XRD characterization and the gas pressure results confirmed crystalline Li_2O_2 as the main discharge product which is consistent with a solution mechanism involved during the discharge process. Also, the ex–situ FEG–SEM observations evidenced that, as a function of the current density, the discharge capacities are dependent on the morphology (toroïds / film) and/or the size distribution of the Li_2O_2 particles in the carbon volume. At higher current densities, the formation of a Li_2O_2 conformal film on all the carbon cathodes is more favored, leading to quite similar capacity. However, at low current densities, the self–standing and binder–free carbon fibers cathode (CF) prepared via electrospinning delivered the highest capacity normalized by the active carbon surface area. This was explained by the homogenous storage of crystalline Li_2O_2 toroïds in the entire carbon volume without any pore blocking probably due to a continuous oxygen diffusion in the 3D macroporous CF structure. In contrast, on the other carbon cathodes, the deposition of Li_2O_2 toroïds with larger diameters occurs preferably at the O_2 rich interface rather than at the electrolyte rich interface. Furthermore, the significant enhancement of the discharge capacity for electrospun cathode at low rates was also found to be correlated to its chemical surface composition and more specifically to the presence of nitrogen species that can act as active sites for discharge and/or nucleation. Thus, the cumulative effect of a larger amount of surface active sites and the more advantageous microstructure of the carbon electrode is the cause of its better performance. This article highlights the importance of the electrospinning process for rational fabrication and engineering of binder-free macroporous carbon materials with higher capacity for battery systems and provides some enlightenment for the air electrode design.

Acknowledgements

The authors thank the ANR through the ECCENTRIC project for financial support. FEG SEM instrumentation was facilitated by the Institut des Matériaux de Paris Centre (IMPC FR2482) and was funded by Sorbonne Université, CNRS and by the C'Nano projects of the Région Ile-de-France. A special thank is addressed to David Montero (IMPC engineer), Ivan T. Lucas (associate professor in Sorbonne Université LISE UMR 8235) and Antoine Miche (LRS engineer) for FEG–SEM, Raman and XPS experiments respectively.

Appendix A. Supplementary data

Supplementary data associated with this article can be found in the online version at:..

References

[1] A. C. Luntz and B. D. McCloskey, Nonaqueous Li–Air Batteries: A Status Report, Chem. Rev. 114 (23) (2014) 11721–11750.

[2] J. Christensen et al., A Critical Review of Li/Air Batteries, J. Electrochem. Soc. 159 (2) (2011) R1-R30.

[3] H. G. Jung, J. Hassoun, J. B. Park, Y. K. Sun, and B. Scrosati, An improved high-performance lithium-air battery, Nat. Chem. 4 (7) (2012) 579-585.

[4] H. J. Kwon *et al.*, Effects of oxygen partial pressure on Li-air battery performance, J. Power Sources 364 (2017) 280-287.

[5] J. W. Jung, C. L. Lee, S. Yu, and I. D. Kim, Electrospun nanofibers as a platform for advanced secondary batteries: A comprehensive review, J. Mater. Chem. A, 4 (2016) 703-750.

[6] Y. Shen *et al.*, A high-capacity lithium-air battery with Pd modified carbon nanotube sponge cathode working in regular air, Carbon N. Y. 62 (2013) 288-295.

[7] L. Zou *et al.*, Bifunctional catalyst of well-dispersed RuO_2 on $NiCo_2O_4$ nanosheets as enhanced cathode for lithium-oxygen batteries, Electrochim. Acta 262 (2018) 97-106.

[8] B. D. McCloskey, R. Scheffler, A. Speidel, D. S. Bethune, R. M. Shelby, and A. C. Luntz, On the efficacy of electrocatalysis in nonaqueous Li-O_2 batteries, J. Am. Chem. Soc., 133 (2011), 18038-18041.

[9] J. J. Xu, Z. W. Chang, Y. Wang, D. P. Liu, Y. Zhang, and X. B. Zhang, Cathode Surface-Induced, Solvation-Mediated, Micrometer-Sized Li_2O_2 cycling for Li–O_2 Batteries, Adv. Mater. 28 (2016) 9620-9628.

[10] A. Nakanishi *et al.*, Electrolyte Composition in Li/O_2 Batteries with LiI Redox Mediators: Solvation Effects on Redox Potentials and Implications for Redox Shuttling, J. Phys. Chem. C 122 (2018) 1522-1534.

[11] W. Liu *et al.*, Intrinsically Optimizing Charge Transfer via Tuning Charge/Discharge Mode for Lithium–Oxygen Batteries, Small, 15 (2019) 1–8.

[12] T. Hsieh, Y. Tsou, and J. Chen, Iron phthalocyanine supported on 3D nitrogen-doped graphene aerogel as an electrocatalyst for non-aqueous Li–O_2 batteries, Electrochim. Acta, 295 (2019) 490-497.

[13] M. Christy, A. Arul, and Y. B. Kim, Carbide composite nanowire as bifunctional electrocatalyst for lithium oxygen batteries, Electrochim. Acta 300 (2019) 186–192.

[14] X. Han, W. Zhang, X. Ma, C. Zhong, N. Zhao, and W. Hu, Identifying the Activation of Bimetallic Sites in $NiCo_2S_4$@g-C_3N_4-CNT Hybrid Electrocatalysts for Synergistic Oxygen Reduction and Evolution, Adv. Mater. 31 (2019) 1808281.

[15] Z. Zhang, X. Li, C. Zhong, N. Zhao, Y. Deng, and X. Han, Spontaneous Synthesis of Silver-Nanoparticle-Decorated Transition- Metal Hydroxides for Enhanced Oxygen Evolution Reaction, Angew. Chem. Int. Ed. 59 (2020) 7245–7250.

[16] X. Han, X. Ling, D. Yu, D. Xie, L. Li, and S. Peng, Atomically Dispersed Binary Co-Ni Sites in Nitrogen-Doped Hollow Carbon Nanocubes for Reversible Oxygen Reduction and Evolution, Adv. Mater. 31 (2019) 1905622.

[17] X. Han, G. He, Y. He, J. Zhang, X. Zheng, and L. Li, Engineering Catalytic Active Sites on Cobalt Oxide Surface for Enhanced Oxygen Electrocatalysis, Adv. Energy Mater. 8 (2018) 1702222.

[18] C. Li *et al.*, A unified mechanism of O_2 reduction in aprotic Li^+-electrolytes and its consequences for Li-O_2 batteries (2014) 1–12.

[19] B. M. Gallant, D. G. Kwabi, R. R. Mitchell, J. Zhou, C. V. Thompson, and Y. Shao-Horn,Influence of Li_2O_2 morphology on oxygen reduction and evolution kinetics in Li-O_2 batteries, Energy Environ. Sci. 6 (2013) 2518–2528.

[20] R. R. Mitchell, B. M. Gallant, Y. Shao-Horn, and C. V. Thompson, Mechanisms of morphological evolution of Li_2O_2 particles during electrochemical growth, J. Phys. Chem. Lett. 4 (2013) 1060–1064.

[21] S. Lau and L. A. Archer, Nucleation and Growth of Lithium Peroxide in the Li-O_2 Battery, Nano Lett. 15 (2015) 5995–6002.

[22] B. Liu, J. Yang, H. Duan, X. Liu, and J. Shui, Cathode Local Curvature Affects Lithium Peroxide Growth in Li-O_2 Batteries, ACS Appl. Mater. Interfaces 11 (2019) 35264–35269.

[23] M. Carboni, S. Brutti, and A. G. Marrani, Surface Reactivity of a Carbonaceous Cathode in a Lithium Triflate/Ether Electrolyte-Based Li-O_2 Cell, ACS Appl. Mater. Interfaces 7 (2015) 21751–21762.

[24] J. Xiao *et al.*, Hierarchically porous graphene as a lithium-air battery electrode, Nano Lett. 11 (2011) 5071–5078.

[25] J. Liu, S. Khaleghi Rahimian, and C. W. Monroe, Capacity-limiting mechanisms in Li/O_2 batteries, Phys. Chem. Chem. Phys. 18 (2016) 22840–22851.

[26] S. Li, M. Wang, Y. Yao, T. Zhao, L. Yang, and F. Wu, Effect of the Activation Process on the Microstructure and Electrochemical Properties of N-Doped Carbon Cathodes in Li-O_2 Batteries, ACS Appl. Mater. Interfaces, 11 (2019) 34997–35004.

[27] Y. Hu, X. Han, F. Cheng, Q. Zhao, Z. Hu, and J. Chen, Size effect of lithium peroxide on charging performance of Li-O_2 batteries, Nanoscale, 6 (2014) 177–180.

[28] X. Ren, S. S. Zhang, D. T. Tran, and J. Read, Oxygen reduction reaction catalyst on lithium/air battery discharge performance, J. Mater. Chem. 21 (2011) 10118–10125.

[29] L. D. Griffith, A. E. S. Sleightholme, J. F. Mansfield, D. J. Siegel, and C. W. Monroe, Correlating Li/O_2 cell capacity and product morphology with discharge current, ACS Appl. Mater. Interfaces, 7 (2015) 7670–7678.

[30] B. Sun, X. Huang, S. Chen, P. Munroe, and G. Wang, Porous graphene nanoarchitectures: An efficient catalyst for low charge-overpotential, long life, and high capacity lithium-oxygen batteries, Nano Lett. 14 (2014) 3145–3152.

[31] P. Tan, L. Shi, W. Shyy, and T. Zhao, Morphology of the Discharge Product in Non-aqueous Lithium-Oxygen Batteries: Furrowed Toroid Particles Correspond to a Lower Charge Voltage, Energy Technol. 4 (2016) 393–400.

[32] C. Xia, M. Waletzko, L. Chen, K. Peppler, P. J. Klar, and J. Janek, Evolution of Li_2O_2 growth and its effect on kinetics of Li-O_2 batteries, ACS Appl. Mater. Interfaces, 6 (2014) 12083–12092.

[33] Z. Qian *et al.*, Insights into the role of oxygen functional groups and defects in the rechargeable nonaqueous Li–O_2 batteries, Electrochim. Acta 292 (2018) 838–845.

[34] H. Han, Y. Jeon, Z. Liu, and T. Song, Highly Graphitic Carbon Nanofibers Web as a Cathode Material for Lithium Oxygen Batteries, Appl. Sci. 8 (2018) 209.

[35] Z. Zhu *et al.*, Effects of various binders on supercapacitor performances, Int. J. Electrochem. Sci., 11 (2016) 8270–8279.

[36] S. N. Arshad, M. Naraghi, and I. Chasiotis, Strong carbon nanofibers from electrospun polyacrylonitrile, Carbon N. Y. 49 (2011) 1710–1719.

[37] N. Kaur, V. Kumar, and S. R. Dhakate, Synthesis and characterization of multiwalled CNT–PAN based composite carbon nanofibers via electrospinning, Springerplus 5 (2016).

[38] X. Huang, Fabrication and properties of carbon fibers, Materials (Basel). 2 (2009) 2369–2403.

[39] F. Lepoivre, A. Grimaud, D. Larcher, and J.-M. Tarascon, Long-Time and Reliable Gas Monitoring in Li-O_2 Batteries via a Swagelok Derived Electrochemical Cell, J. Electrochem. Soc. 163 (2016) A923–A929.

[40] Y. Devrim, S. Erkan, N. Baç, and I. Eroglu, Improvement of PEMFC performance with Nafion/inorganic nanocomposite membrane electrode assembly prepared by ultrasonic coating technique, Int. J. Hydrogen Energy, 37 (2012) 16748–16758.

[41] N. Mahne, O. Fontaine, M. O. Thotiyl, M. Wilkening, and S. A. Freunberger, Mechanism and performance of lithium-oxygen batteries-a perspective, Chem. Sci., 8 (2017) 6716–6729.

[42] Z. Lyu *et al.*, Recent advances in understanding of the mechanism and control of Li_2O_2 formation in aprotic Li-O_2 batteries, Chem. Soc. Rev. 46 (2017) 6046–6072.

[43] S. Ganapathy *et al.*, Nature of Li_2O_2 oxidation in a Li-O_2 battery revealed by operando X-ray diffraction, J. Am. Chem. Soc. 136 (2014) 16335–16344.

[44] L. Wang, Y. Zhang, Z. Liu, L. Guo, and Z. Peng, Understanding oxygen electrochemistry in aprotic Li–O_2 batteries, Green Energy Environ. 2 (2017) 186–203.

[45] Y. Wang, N. C. Lai, Y. R. Lu, Y. Zhou, C. L. Dong, and Y. C. Lu, A Solvent-Controlled Oxidation Mechanism of Li_2O_2 in Lithium-Oxygen Batteries, Joule, 2 (2018) 2364–2380.

[46] B. M. Gallant, D. G. Kwabi, R. R. Mitchell, J. Zhou, C. V Thompson, and Y. Shao-horn, Environmental Science evolution kinetics in Li –O_2 batteries, (2013) 2518–2528.

[47] B. D. Adams, C. Radtke, R. Black, M. L. Trudeau, K. Zaghib, and L. F. Nazar, Current density dependence of peroxide formation in the Li-O_2 battery and its effect on charge, Energy Environ. Sci. 6 (2013) 1772–1778.

[48] I. Bardenhagen, M. Fenske, D. Fenske, A. Wittstock, and M. Bäumer, Distribution of discharge products inside of the lithium/oxygen battery cathode, J. Power Sources, 299 (2015) 162–169.

[49] K. B. Knudsen, A. C. Luntz, S. H. Jensen, T. Vegge, and J. Hjelm, Redox Probing Study of the Potential Dependence of Charge Transport Through Li_2O_2, J. Phys. Chem. C, 119 (2015) 28292–28299.

[50] K. B. Knudsen, T. Vegge, B. D. McCloskey, and J. Hjelm, An electrochemical impedance spectroscopy study on the effects of the surface and solution-based mechanisms in Li-O_2 cells, J. Electrochem. Soc. 163 (2016) A2065–A2071.

[51] T. Sharifi *et al.*, Nitrogen doped multi walled carbon nanotubes produced by CVD-correlating XPS and Raman spectroscopy for the study of nitrogen inclusion, Carbon N. Y., 50 (2012) 3535–3541.

[52] C. V. Rao, C. R. Cabrera, and Y. Ishikawa, In search of the active site in nitrogen-doped carbon nanotube electrodes for the oxygen reduction reaction, J. Phys. Chem. Lett., 1 (2010) 2622–2627.

[53] J. Wu, Z. Pan, Y. Zhang, B. Wang, and H. Peng, The recent progress of nitrogen-doped carbon nanomaterials for electrochemical batteries, J. Mater. Chem. A, 6 (2018) 2932–12944.

[54] K. Sakai, S. Iwamura, R. Sumida, I. Ogino, and S. R. Mukai, Carbon paper with a high surface area prepared from carbon nanofibers obtained through the liquid pulse injection technique, ACS Omega, 3 (2018) 691–697.

Figures captions

Fig. 1. (a) Full discharge voltage profiles of the electrospun carbon electrode at different discharge rates. Variation of the full discharge capacities reached for the different carbon materials as a

function of current density applied in Li–O_2 cells using 0.1 M $LiPF_6$ in DME. The capacities values were normalized by (b) the total carbon cathode weight (g_c) or (c) the geometric cathode surface (0.64 cm^2) or (d) the active surface area (m_c^2) calculated on the basis of the estimated surface area ($m^2.g^{-1}$) in table 1 and the carbon weight (g_c).

Fig. 2. (a) XRD patterns of the cathodes after full discharge at 0.05 $mA.cm^{-2}_{(geom)}$. (b) Gas evolution profiles of Li-O_2 cells at low current density of 0.05 $mA.cm^{-2}_{(geom)}$ using 0.1 M $LiPF_6$ in DME, the ratio of number of electrons to oxygen is very close to 2.

Fig. 3. (a) Morphology of Li_2O_2 products formed at the O_2/cathode interfaces during full discharge step of carbon materials in Li-O_2 cells at different current densities using 0.1 M $LiPF_6$ in DME. (b) Representative microscopic images of fully discharged GDL cathode regardless of the current density applied in the cell.

Fig. 4. Distribution of Li_2O_2 products formed through the carbon cathode volume during full discharge step in Li-O_2 cells at low current density of 0.05 $mA.cm^{-2}_{(geom)}$.

Fig. 5. (a) Full discharge voltage profiles of electrospun carbon fibers (CF_10% PAN) with different thicknesses in Li-O_2 cells operating at 0.05 $mA.cm^{-2}_{(geom)}$) using 0.1 M $LiPF_6$ in DME. (b) FEG–SEM analyses of the fully discharged 600 µm-CF cathode.

Fig. 6. (a) XPS spectra of the different carbon electrodes with the related surface chemical composition. The binding energies for carbon, nitrogen and oxygen are 284.8, 389.32 and 533 eV, respectively. (b) XPS deconvolution of N1s peaks of carbon cathodes before discharge. N-1, N-2 and N-3 correspond to Pyridinic-N (BE = 398.3 eV), Pyrrolic-N (BE = 400.9 eV) and Graphitic–N (BE = 403.5 eV), respectively. (c) XPS analysis of the C1s region in carbon materials before discharge showing different chemical bonds sp^3, sp^2 and oxygen species present in different relative proportions. Carbon sp^2 (BE= 284.8 eV), carbon sp^3 (BE= 285.7 eV), C-O (BE=287.7 eV), C=O and/or C=N (BE= 289 eV) and shake up π-π* (BE=290.7 eV). The peak lineshapes used were Voigt functions, i.e. Gaussian–Lorentzian convolutions, with an integral background subtracted prior to fitting. The peaks assignments were based on models discussed in [51].

Tables Captions

Table 1
Surface and porosity characteristics of pristine carbon electrodes.

Table 2
Electronic conductivities values of carbon electrodes.

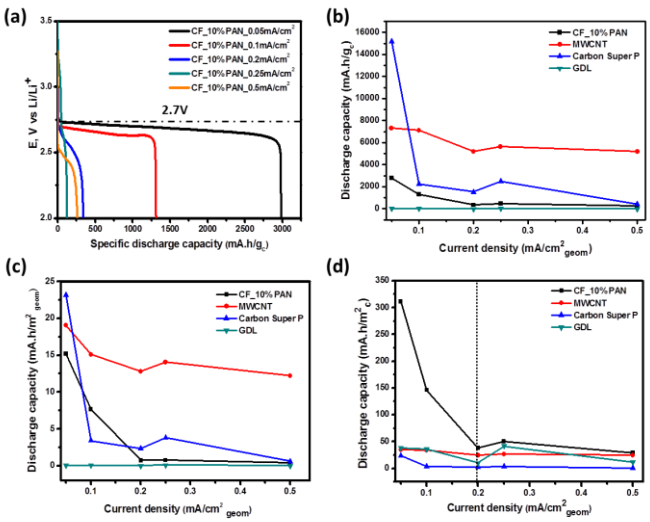

Fig. 1. (a) Full discharge voltage profiles of the electrospun carbon electrode at different discharge rates. Variation of the full discharge capacities reached for the different carbon materials as a function of current density applied in Li–O_2 cells using 0.1 M $LiPF_6$ in DME. The capacities values were normalized by (b) the total carbon cathode weight (g_c) or (c) the geometric cathode surface (0.64 cm^2) or (d) the active surface area (m_c^2) calculated on the basis of the estimated surface area ($m^2.g^{-1}$) in table 1 and the carbon weight (g_c).

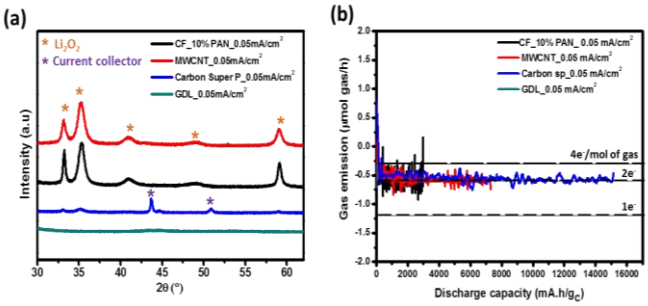

Fig. 2. (a) XRD patterns of the cathodes after full discharge at 0.05 $mA.cm^{-2}_{(geom)}$. (b) Gas evolution profiles of Li-O_2 cells at low current density of 0.05 $mA.cm^{-2}_{(geom)}$ using 0.1 M $LiPF_6$ in DME, the ratio of number of electrons to oxygen is very close to 2.

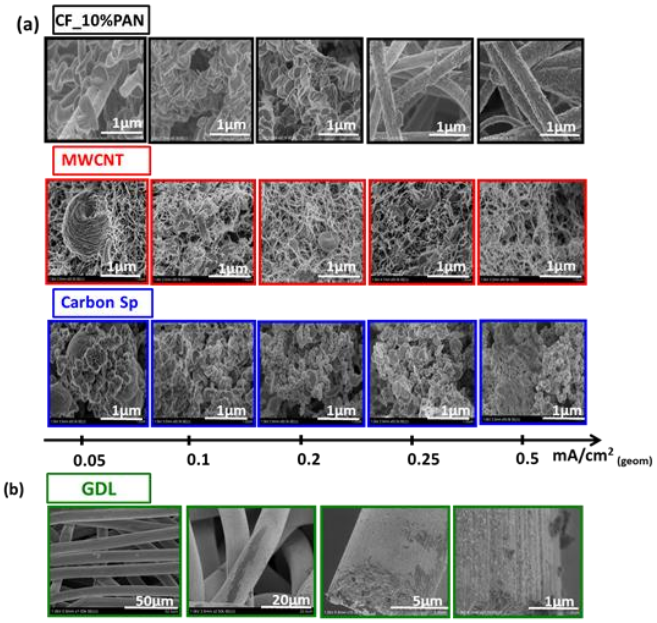

Fig. 3. (a) Morphology of Li_2O_2 products formed at the O_2/cathode interfaces during full discharge step of carbon materials in Li-O_2 cells at different current densities using 0.1 M $LiPF_6$ in DME. (b) Representative microscopic images of fully discharged GDL cathode regardless of the current density applied in the cell.

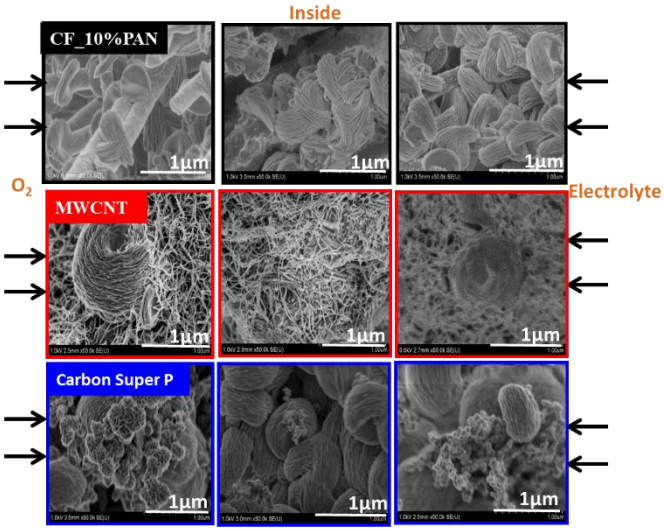

Fig. 4. Distribution of Li_2O_2 products formed through the carbon cathode volume during full discharge step in Li-O_2 cells at low current density of 0.05 mA.$cm^{-2}_{(geom)}$.

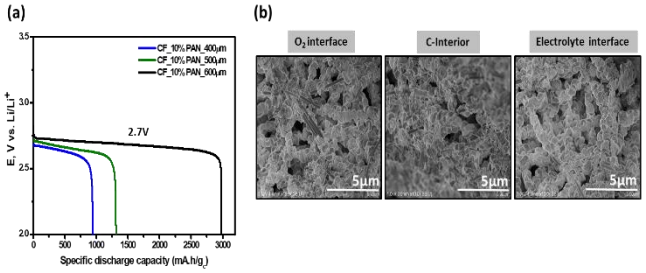

Fig. 5. (a) Full discharge voltage profiles of electrospun carbon fibers (CF_10% PAN) with different thicknesses in Li-O_2 cells operating at 0.05 mA.cm^{-2} $_{(geom)}$) using 0.1 M $LiPF_6$ in DME. (b) FEG–SEM analyses of the fully discharged 600 µm–CF cathode.

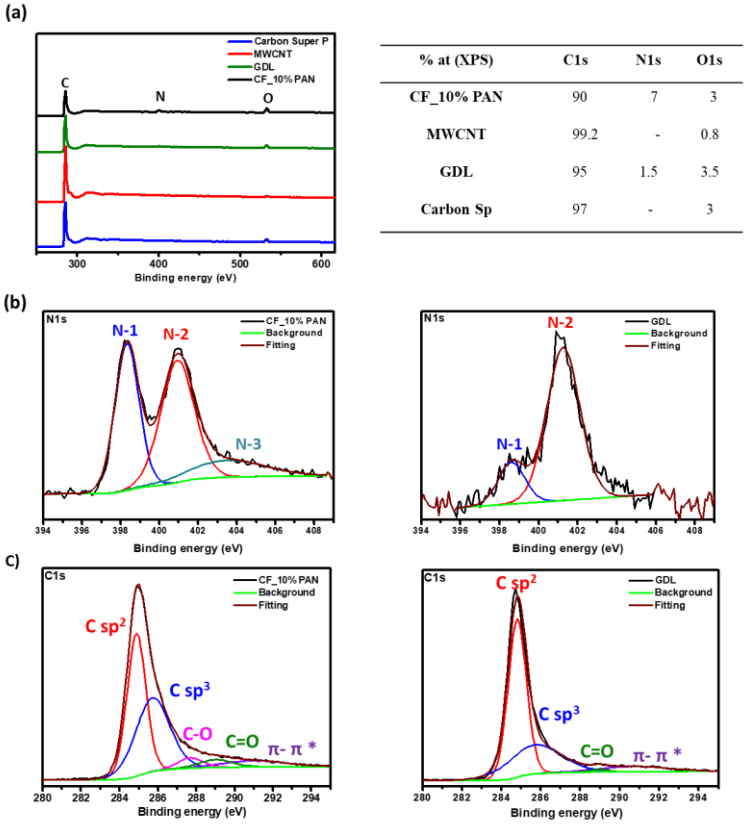

% at (XPS)	C1s	N1s	O1s
CF_10% PAN	90	7	3
MWCNT	99.2	-	0.8
GDL	95	1.5	3.5
Carbon Sp	97	-	3

Fig. 6. (a) XPS spectra of the different carbon electrodes with the related surface chemical composition. The binding energies for carbon, nitrogen and oxygen are 284.8, 389.32 and 533 eV, respectively. (b) XPS deconvolution of N1s peaks of carbon cathodes before discharge. N-1, N-2 and N-3 correspond to Pyridinic-N (BE = 398.3 eV), Pyrrolic-N (BE = 400.9 eV) and Graphitic–N (BE = 403.5 eV), respectively. (c) XPS analysis of the C1s region in carbon materials before discharge showing different chemical bonds sp^3, sp^2 and oxygen species present in different relative proportions. Carbon sp^2 (BE= 284.8 eV), carbon sp^3 (BE= 285.7 eV), C-O (BE=287.7 eV), C=O and/or C=N (BE= 289 eV) and shake up π-π* (BE=290.7 eV). The peak lineshapes used were Voigt functions, i.e. Gaussian–Lorentzian convolutions, with an integral background subtracted prior to fitting. The peaks assignments were based on models discussed in [51].

Table 1
Surface and porosity characteristics of pristine carbon electrodes.

Carbon samples	Fibers size (nm)[1]	Surface area $_c$ ($m^2.g^{-1}$)[2]	Porosity $_{theo}$ (%)[3]	V_{micro} (d<2nm) ($cm^3.g^{-1}$)[4]	V_{meso} (2<d<50nm) ($cm^3.g^{-1}$)[4]	V_{meso} (50nm<d) ($cm^3.g^{-1}$)[5]	V_{macro} (50<d<100nm) ($cm^3.g^{-1}$)[5]	V_{macro} (50<d<200nm) ($cm^3.g^{-1}$)[5]	V_{macro} (d>200nm) ($cm^3.g^{-1}$)[5]	Pores size (µm)[5]	Electrolyte uptake %
CF-10%PAN	260±30	9	96	0.06	0.05	0	0	0	34.8	1-1.5	550
GDL	10000±900	0.21	70	0	0.009	0	0	0.003	2.2	0.2-50	114
MWCNT	10±2	210	88	0.05	0.17	0.27	0.25	0.63	2.7	0.008-0.2	490
Carbon Super P (powder)	60±0.3	62	76	0.001	0.012	0.01	0.48	0.61	5.2	0.07-0.1	-

[1] Measured by SEM images using image J software
[2] Calculated from the fibers diameter observed from SEM images and the true density of carbon (2g.cm^{-3}) assuming that all the fibers are uniform cylinders. Only the surface area of the carbon Super P bulk powder is estimated by BET measurements.
[3] Calculated by the equation $\varepsilon = 1 - (4m / \pi\rho_c d2L)$ (ε: porosity, m: weight of the sample, ρ_c: true density of carbon = 2g.cm^{-3}, d: diameter of the sample, L: thickness of the sample))[54] except for the Carbon Super P powder which porosity % is calculated by BET method.
[4] Obtained after applying the DFT method to the N_2 adsorption isotherm data
[5] Estimated by mercury porosimetry measurements.

Table 2

Electronic conductivities values of carbon electrodes.

Carbon samples	Resistivity R sheet (Ω.cm) [1]	Conductivity (S.cm^{-1}) [2]
CF-10%PAN-950°C	100-400	0.5 10^{-2}
GDL	2-5	5 10^{-2}
MWCNT	5-10	0.6 10^{-2}
Carbon Super P	-	-

[1] *Results from four probe conductivity experiments.*

[2] *Calculated using Impedance measurements (see Fig. S10).*